Protein Design Provides Lead(II) Ion Biosensors for Imaging Molecular Fluxes around Red Blood Cells[†]

Vivekanand S. Shete[‡] and David E. Benson[§,*]

Department of Chemistry, Wayne State University, Detroit, Michigan 48202, and Departments of Chemistry and Biochemistry, Calvin College, Grand Rapids, Michigan 49546

Received September 17, 2008; Revised Manuscript Received November 17, 2008

ABSTRACT: Metalloprotein design and semiconductor nanoparticles have been combined to generate a reagent for selective fluorescence imaging of Pb^{2+} ions in the presence red blood cells. A biosensor system based on semiconductor nanoparticles provides the photonic properties for small molecule measurement in and around red blood cells. Metalloprotein design was used to generate a Pb^{2+} ion selective receptor from a protein that is structurally homologous to a protein used previously in this biosensing system. Parameters for the Pb^{2+} ion binding site were derived from crystallographic structures of low molecular weight Pb^{2+} ion complexes that contain a stereoactive lone pair. When the designed protein was produced and attached to ZnS-coated CdSe nanoparticles, two $Pb(NO_3)_2$-associated binding events were observed (2-fold emission decrease; $K_{A1} = 1 \times 10^9\ M^{-1}$; $K_{A2} = 3.5 \times 10^6\ M^{-1}$). The fluorescence response had a 100 pM $Pb(NO_3)_2$ detection limit, while no response was observed with Ca^{2+} ions (10 mM), Zn^{2+} ions (100 μM), or Cd^{2+} ions (100 μM). Metal ion selectivity presumably comes from the coordination geometry selected to favor lone pair formation on Pb^{2+} ions and electrostatically disfavor tetrahedral coordination. Replacement of ZnS-coated CdSe with ZnS-coated InGaP nanoparticles provided similar biosensors (100 pM limit of detection; $K_{A1} = 1 \times 10^9\ M^{-1}$; $K_{A2} = 1 \times 10^7\ M^{-1}$) but with excitation/emission wavelengths longer than the major absorbance of red blood cell hemoglobin (>620 nm). The InGaP nanoparticle-based biosensors provided a 5 nM $Pb(NO_3)_2$ detection limit in the presence of red blood cells. The modularity of the biosensor system provides exchangeable Pb^{2+} ion detection around red blood cells.

Over 2% of children in the United States from 1999 to 2001 (~400000) had Pb^{2+} ion levels in blood (PbB levels) above 10 μg/dL, or 0.5 μM (*1*). Individuals with these PbB levels display slowed motor responses, decreased IQs, and hypertension. Chelation therapy is used to treat lead intoxication; however, it is ineffective below moderate PbB levels (40 μg/dL, 1.9 μM). A current rationale for this inefficacy is that Pb^{2+} ion exchange between bone, blood, and tissue is slow (*2*). This rationale is supported by ICP-MS studies that show while PbB levels are at 40 μg/dL, plasma Pb^{2+} ion concentrations are at 13 nM (*3*). This finding highlights the central role of red blood cells in sequestering and delivering Pb^{2+} ions from bone tissue through the blood stream and to various tissues (e.g., brain). While liposome models have been developed to study the equilibrium effects of ionophores that catalyze Pb^{2+} ion exchange (*2*), fluorescent probes for spatial and time-dependent variations, termed fluxes (*4*), of exchangeable Pb^{2+} ion concentrations within red blood cells need to be developed. Such an imaging application would not only distinguish between exchangeable and total Pb^{2+} ion concentrations but also determine cellular structure(s) responsible for import and release of exchangeable Pb^{2+} ions for red blood cells. Toward this end, organic fluorophores and green fluorescent protein chimeric proteins have been developed to monitor small molecule fluxes in plant and mammalian cells (*5, 6*). For molecular imaging of red blood cells, current fluorophores for Pb^{2+} ion analysis emit at wavelengths that are obscured by the heme *b* absorbance of hemoglobin, and alternative fluorophores need to be used.

Semiconductor nanoparticles (quantum dots) provide a solution to fluorescence sensing in and around red blood cells. Depending on the radius of and/or material comprising the semiconductor nanoparticle, the excitation and emission wavelengths can be tuned far into the near-infrared region (*7*). The quantum yields, photostability, emission line width, and emission wavelength tunability are far superior to red fluorescent proteins and red-emitting organic fluorophores (*8*). In addition, coating these nanoparticles with two to three monolayers of ZnS improves the fluorescence properties and creates a barrier between the nanoparticle and the biological system (*9*). The synthesis and production of certain semiconductor nanoparticles have progressed to the point of commercially available preparations. While much controversy still surrounds the toxicity of ZnS-coated CdSe (CdSe@ZnS) nanoparticles, ZnS-coated InGaP (InGaP@ZnS) nanoparticles have minimal toxicity (*10*). Other "green"

[†] The authors acknowledge funding from the National Science Foundation (DBI-0508134), the National Institute for Environmental Health Sciences pilot project grant (ES06639), and the Office of Naval Research (N000140710218).

* To whom correspondence should be addressed: phone, (616) 526-7699; fax, (616) 526-6501; e-mail, dbenson@calvin.edu.

[‡] Current address: Department of Chemistry, The Ohio State University, 1043 Evans Laboratory, 100 West 18th Ave., Columbus, OH 43210-1185.

[§] Calvin College.

10.1021/bi801777h CCC: $40.75
Published on Web 12/19/2008

Scheme 1: Biosensing Approach and Modularity[a]

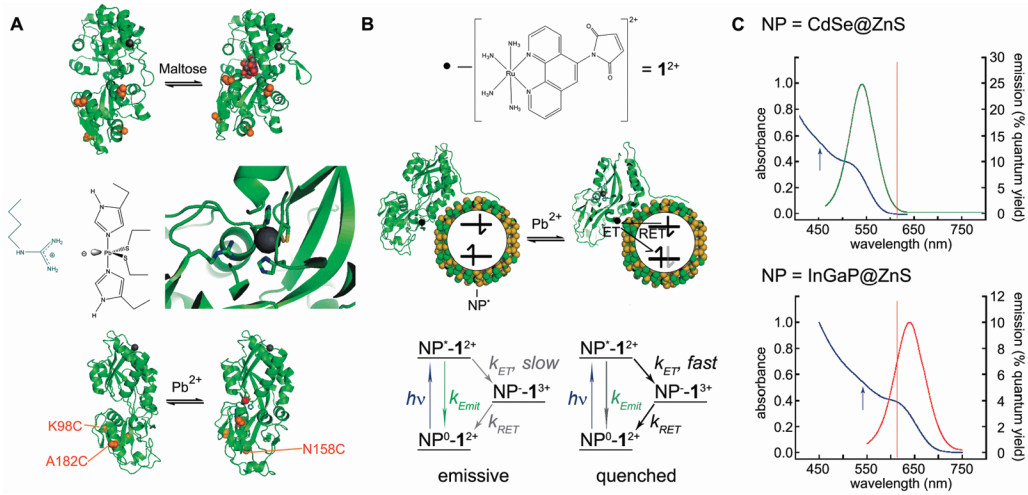

[a] Nanoparticle-based biosensors are comprised of three aspects: (A) analyte-mediated change in protein conformation (top, MBP; middle, Pb^{2+} ion binding site design parameters and predicted Pb^{2+} ion binding site; bottom, PBP•Pb^{2+}; orange residues, surface Cys for maleimide attachment; gray balls, carboxy terminus where MT domain is fused), (B) electron transfer reaction from a maleimide-functionalized metal complex (**1**, top) and semiconductor nanoparticle (NP) controlled by the protein conformation (middle), where fast electron transfer quenches nanoparticle emission (bottom), and (C) semiconductor nanoparticles used here (red line, red blood cell band-pass; arrows, excitation wavelength).

semiconductor nanoparticles have been developed where Mn^{2+} ions are doped into nontoxic ZnSe nanoparticles (*11, 12*) but do not provide the spectral properties needed for fluorescence detection in red blood cells. This report demonstrates that commercially available InGaP@ZnS nanoparticles (*13*) can provide small molecule biosensing around red blood cells. It should be noted that recently the synthesis of larger InP@ZnS nanoparticles has been reported that are excited and emit at even longer emission wavelengths (*14*). More importantly, this provides an avenue into fluorescent biosensors that utilize other semiconductor nanoparticles for studying molecular fluxes in red blood cells and for deep tissue imaging.

While there are Pb^{2+} ion-dependent fluorophores (*15*), peptides (*16*), and transcription factors (*17*), these systems are not readily adaptable for use with semiconductor nanoparticles. It should be noted that Pb^{2+} ion analysis in biological media can be performed using anodic striping voltammetry or atomic absorption; however, these techniques are not amenable to imaging applications. Imaging Pb^{2+} ion fluxes requires a reversible and unimolecular detection scheme. RNA-modified gold nanoparticles (*46, 47*) could be adapted to semiconductor nanoparticles; however, the irreversible Pb^{2+} ion-dependent cleavage reaction that facilitates detection makes this sensor nonadaptable for real-time fluorescence imaging. Organic fluorophores (*15*), peptides (*16*), and transcription factors (*17*) that show Pb^{2+}-dependent changes in emission intensity currently emit at wavelengths that would be obscured by the major absorbance of hemoglobin. For highly absorbant/emissive chromophores (ε_{ex} > 100000 M^{-1} cm^{-1}; quantum yield >5%), we estimate excitation and emission wavelengths longer than 620 nm ($\varepsilon_{hemoglobin}$ < 5000 M^{-1} cm^{-1}) (*18*) are necessary for detection with red blood cells. This criterion even rules out red-emitting versions of green fluorescent protein. Two systems are known that provide analyte-dependent changes in semiconductor nanoparticle emission in biological buffers. These systems are based on analyte-mediated conformation change (*20, 39*) and binding pocket solvation changes (*19*).

Here we use metalloprotein design tools to extend this semiconductor nanoparticle-based biosensing strategy to detecting exchangeable Pb^{2+} ion concentrations in and around red blood cells. Protein design techniques have been shown (*26*) to adapt native ligand binding sites to selectively bind an alternative, noncognate ligand of choice. For this study we have surveyed the previously employed (*20*) maltose binding protein (MBP)[1] and four structurally homologous proteins for adaptation to Pb^{2+} ion binding. Phosphate binding protein (PBP) was selected for redesign. The periplasmic binding protein superfamily has not only been used for developing fluorescent biosensors (*21*) but has also been used as scaffold proteins for protein design (*49*). The Pb^{2+} ion-binding protein (PBP•Pb^{2+}) was generated using protein design tools in concert with known parameters from metalloprotein design (*26*) and metal complex crystallographic analysis (*28, 29, 50*). The designed protein was then integrated into the MBP-based semiconductor nanoparticle biosensor system (Scheme 1). Use of commercially available InGaP@ZnS nanoparticles provided a Pb^{2+} ion biosensor that functioned in the presence of red blood cells. The Pb^{2+} ion biosensor provided by this process has detection limits and spectral properties that will enable fluxomic analysis of red blood cells to address lead poisoning.

MATERIALS AND METHODS

All chemicals, unless otherwise noted, were used without additional purification. Rabbit red blood cells were collected

[1] Abbreviations: MBP, maltose binding protein; PBP, phosphate binding protein; PBP•Pb^{2+}, G140H, F11H, A9C, D56C, T114G, S38G PBP; **1** or complex **1**, [Ru(5-maleimido-1,10-phenanthroline)$(NH_3)_4$]-(PF_6); MHDA, 16-mecaptohexadecanoic acid; MOPS, 3-(*N*-morpholino)propanesulfonic acid; MT, metallothionein; PBP•Pb^{2+}-MT, PBP•Pb^{2+} with metallothionein encoded on the carboxy terminus; CFP, cyan fluorescent protein; YFP, yellow fluorescent protein; SALP, stereochemically active lone pair.

by Prof. Dana Spence's laboratory, and additional manipulations at Wayne State University were performed using IACUC approved practices.

Protein and Biosensor Preparation. Proteins were produced by *Escherichia coli* overexpression from plasmid DNA and purified to homogeneity using polyhistidine domain affinity chromatography (*19*). The polyhisititidine domain was removed from proteins using an enterokinase digestion and repurification (*22*). $[Ru(L)(NH_3)_4](PF_6)_2$ (**1**, L = 5-maleimido-1,10-phenanthroline) was synthesized and attached to the proteins using reported procedures (*20, 39,*). Hexadecylamine-capped CdSe@ZnS (NN Laboratories, Fayetteville, AK) and trioctylphosphine oxide capped InGaP@ZnS nanoparticles (Evident Technologies, Troy, NY) were exchanged with 16-mercaptohexadecanoic acid to provide water-soluble nanoparticles with minimal capping group exchange (*23*). The proteins were adsorbed to MHDA-capped CdSe@ZnS or InGaP@ZnS nanoparticles in 50 mM MOPS (pH 7.5) through an engineered cysteine-rich, carboxy-terminal protein domain (MT) after 1 h of reaction (*20, 39*). Peptides based on the MT domain were produced as reported (*24*) and exchanged with MHDA-capped, protein-attached CdSe@ZnS or InGaP@ZnS nanoparticles for 1 h (room temperature) followed by dialysis (20000 MW cutoff; Slide-A-Lyzer, Pierce). The generated biosensor was used immediately after dialysis.

Lead Receptor Design and Production. The Site Search algorithm in Dezymer (*51*) was used to predict amino acid side chain replacements that would provide the desired Pb^{2+} ion coordination sphere in MBP or structurally homologous protein. Five structurally characterized members of the bacterial periplasmic binding protein family were used in the search (Supporting Information). The geometric parameters for the Pb^{2+} ion selective coordination sphere (Scheme 1, Supporting Information) were input to the Dezymer program and analyzed by visually inspecting the predicted structures using Prekin/Mage software (*25*). A $PbHis_2Cys_2$ coordination sphere with axial histidines was predicted from the G140H, F11H, A9C, D56C set of mutations to PBP (*36*) (Scheme 1A). The mutations T114G and S38G were added ($PBP{\cdot}Pb^{2+}$) to reduce steric clashes between these side chains and either the Pb^{2+} ion or coordinating side chains. The coding DNA for $PBP{\cdot}Pb^{2+}$ was ordered from Midland Certified Reagent Co., Inc. (Midland, TX), PCR amplified, and ligated into vector DNA that coded for the maltose binding protein−metallothionein fusion (*23*), to generate $PBP{\cdot}Pb^{2+}$-MT. Restriction nuclease sites were used to direct this exchange (5′, *Sal*I; 3′, *Pst*I). An additional double-stranded piece of DNA was introduced to the *Pst*I restriction site to provide a stop codon before the metallothionein coding sequence on a second plasmid ($PBP{\cdot}Pb^{2+}$). The plasmid coding for the $PBP{\cdot}Pb^{2+}$-MT was mutated to code for Cys at positions 98 (K98C $PBP{\cdot}Pb^{2+}$-MT), 158 (N158C $PBP{\cdot}Pb^{2+}$-MT), and 182 (A182C $PBP{\cdot}Pb^{2+}$-MT) using QuikChange mutagenesis and verified using dideoxy DNA sequencing (University of Michigan School of Medicine).

Circular Dichrosim. Protein samples (5 μM, 1 cm cuvette) were examined in a 20 mM phosphate buffer (pH 7.5) to minimize absorbance from 190 to 230 nm. Circular dichroism spectra were recorded (Applied Photophysics) or monitored at 222 nm as temperature was varied (Peltier controller).

Absorbance Spectrophotometry. Standard quartz 1 mL, 1 cm path length cuvettes (NSG Precision cells) were used with or without a screw cap and Teflon septum to maintain an anaerobic environment. Anaerobicity, when necessary, was maintained by sample preparation inside an anaerobic bag (Coy Laboratory Products, Grass Lake, MI) or by degassing while connected to an argon manifold with gastight syringes for sample transfer. Samples were examined with a Hitachi U-2000 spectrophotometer (1 nm slit width).

Fluorescence Spectophotometry. Fluorescence measurements were performed with a Spex Fluorolog-3 fluorometer was used with a 1 s integration time and 3 nm slit widths for buffer experiments and 20 nm slit widths for red blood cell experiments. A 1 mL solution (buffer-based measurements, quartz cuvette) or 1.8 mL solution (red blood cell experiments, 3 mL plastic cuvette) of each biosensor was examined at 25 °C (∼1−2 min equilibration time) under constant stirring (Cuv-o-Stir; Hellma). The red blood cell solutions were prepared from a concentrated stock of red blood cells (50−70% hematocrit) through dilution to a 1% hematocrit in 50 mM MOPS, pH 7.5.

Pb^{2+} Ion Titration and Fitting of Binding Isotherms. Dissociation constants for Pb^{2+} ion binding to $PBP{\cdot}Pb^{2+}$-MT protein were determined by fluorometric titration studies in 50 mM MOPS, pH 7.5. Six different Pb^{2+} ion solutions were prepared with different concentrations with a total volume of 1 mL. The Pb^{2+} ion stock solution was purchased as an atomic absorption standard (Sigma-Aldrich, St. Louis, MO). The six stock solutions were prepared by diluting this 1000 ppm stock solution to various concentrations (1 mM, 100 μM, 10 μM, 1 μM, and 0.1 μM). The resulting solutions were filtered, and the concentration was confirmed by atomic absorbance spectroscopy. The measured concentrations were within 10% of the perceived concentration. Emission or absorbance spectra were collected for the $PBP{\cdot}Pb^{2+}$ samples without the Pb^{2+} ions until a stable spectrum was obtained. To this was added a certain volume, typically 1 μL, of the lowest concentration (0.1 μM) of Pb^{2+} ions, the sample was mixed, and the spectrum was collected. The association constants were calculated by creating a scatter plot (IgorPro; WaveMetrics, Portland, OR) of the fractional saturation versus the Pb^{2+} ion concentration. Fractional saturation (F) was calculated using the difference between the initial and saturated biosensor fluorescence response. A dual binding event isotherm was used for the association constant determination and fit in IgorPro:

$$F = (A_1[Pb(NO_3)_2])/((1/K_{A1})[Pb(NO_3)_2]) + ((1 - A_1)[Pb(NO_3)_2])/((1/K_{A2}) + [Pb(NO_3)_2]) \quad (1)$$

where A_1 is the amplitude of the high-affinity phase, K_{A1} is the association constant of the high-affinity phase, $(1 - A_1)$ is the amplitude of the weaker affinity phase (A_2), and K_{A2} is the association constant for the weaker affinity phase.

Fluorescence Microscopy. An Olympus IX-71 inverted fluorescence microscope (60× objective; Q-Imaging Rolera XR CCD) was used to examine red blood cell samples (1% hematocrit, as above). Bright field images were observed with the standard light source while fluorescence images were detected with the Xe arc light source and a Cy5 filter cube (Chroma Technologies, 41009) using a 10 s acquisition time.

RESULTS AND DISCUSSION

Protein Design. Metalloprotein design has emerged as a powerful tool to understand biomolecular control of coordination chemistry (*26*) and generate biotechnologically related reagents (*27*). Stereochemically active lone pair (SALP) formation is unique to reduced oxidation states of heavier *p*-block ions (*28*), such as Pb^{2+} ions. Here, a coordination sphere was selected to favor SALP formation in a coordinated Pb^{2+} ion but exclude other coordinatively saturated geometries (trigonal planar, tetrahedral, trigonal bipyramidal, octahedral, etc.) Such a coordination sphere should confer Pb^{2+} ion selectivity relative to Ca^{2+}, Zn^{2+}, and Cd^{2+} ions (*29*). Structural discrimination similar to this has been observed with pendent-tetraazacyclononane ligands (*30*), where a Pb^{2+} complex showed an asymmetric coordination while the Hg^{2+} complex was spherically coordinated. Recently, a Pb^{2+} ion-dependent transcription factor seems to bind Pb^{2+} ions and form a SALP (*31*), which could provide metal ion specificity. One report has summarized crystallographic database entries for low molecular weight lead complexes and found coordination modes with a high percentage of hemidirected (SALP-containing) coordination geometries (*50*). We have defined geometric constraints from Pb^{2+} ion coordination complexes as input parameters (Supporting Information) for protein redesign. Four-coordinate geometries were selected over previously examined three-coordinate geometries (*32*) to increase the enthalpic energy driving domain−domain closure and Pb^{2+} ion binding. An additional rationale against designing a three-coordinate site comes from the recent structure of CmtR (*63*), which coordinates Cd^{2+} and Pb^{2+} ions (*33*) and shows a Cd^{2+} ion coordinated in a trigonal Cys_3 fashion. It should be noted that the trigonal Pb^{2+} ion coordination site can be designed in three helical bundles (*32*); however, the ionic size selectivity conferred by such a strategy is not readily adaptable to more flexible proteins, especially binding sites at domain−domain interfaces.

The Dezymer algorithm (*51*) was used to predict mutations that provide a Pb^{2+} ion binding site in five periplasmic binding proteins. The periplasmic binding protein superfamily is bidomain proteins that undergo a ligand-dependent hinge-bending motion that has been linked to changes in organic fluorophore emission, YFP/CFP energy transfer, electrochemical detection, and semiconductor nanoparticle emission (*21*). For the Dezymer predictions, the geometric parameters for the primary coordination sphere were specified with relatively tight parameters and moderate conformational sampling of liganding side chains. Parameters for a four-coordinate, hemidirected Pb^{2+} ion coordination sphere with slightly shorter equatorial than axial bond lengths (Scheme 1A, middle) were supplied to Dezymer. Two configurations were examined (axial bis-Cys and axial bis-His) in maltose-bound maltose binding protein (*34*) and the ligand-bound structures of four structurally related proteins (Supporting Information). All of these proteins provide the first step in bacterial chemosensing for the cognate ligands (*35*) and could replace maltose binding protein in CdSe@ZnS nanoprticle-based maltose biosensors (*20, 39*). Predicted mutation sets (sites) from each protein were evaluated visually for the following properties: protein destabilization, Pb^{2+} ion-mediated domain−domain closure, and SALP electrostatic stabilization. A site in phosphate binding protein (*36*) was selected for construction with two additional mutations to remove Pb^{2+} ion steric clashes (G140H, F11H, A9C, D56C, T114G, S38G phosphate binding protein, PBP•Pb^{2+}; Scheme 1A, middle), which contained Arg 135 with $N_{\eta 1}$ and $N_{\eta 2}$ around 5 Å from the Pb^{2+} ion. While Pb^{2+} ion SALP−Arg 135 electrostatic interaction is not expected to provide affinity, this interaction could provide selectivity over other metal ions. For example, removal of a pendent negative charge in trispicolinate ligands compared to bispicolinate ligands increased the Pb^{2+} ion selectivity over Ca^{2+} ions by 1000-fold (*37*). DNA encoding PBP•Pb^{2+} was inserted into two *E. coli* expression plasmids, which provided either PBP•Pb^{2+}, for electronic absorbance, or PBP•Pb^{2+}-MT, for attachment to semiconductor nanoparticles. Both of these proteins were purified by the amino-terminal $(His\text{-}Gln)_6$ fusion peptide that was proteolyzed and removed by immobilized metal affinity chromatography.

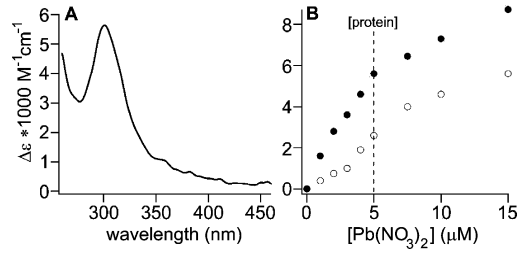

FIGURE 1: Optical absorbance of Pb^{2+}-bound PBP•Pb^{2+} (5 μm). (A) Spectrum of 1:1 Pb^{2+}/PBP•Pb^{2+}. (B) Pb^{2+} titration data for PBP•Pb^{2+} in the absence (filled circles) and presence (open circles) of 10 mM $CaSO_4$.

The function of the designed PBP•Pb^{2+} protein was validated using absorbance techniques. Circular dichroism demonstrated that the relative α-helical content was not altered from phosphate binding protein at room temperature. Thermal denaturation studies (monitored at 222 nm) showed a decrease in thermal stability (82 to 52 °C) upon the addition of six amino acid side chain substitutions. Addition of $Pb(NO_3)_2$ to PBP•Pb^{2+} in bis(2-hydroxyethyl)iminotris(hydroxylmethyl)methane (bis-tris, pH 7.5) formed an absorbance band at 300 nm (Figure 1). The extinction coefficient of this band ($\varepsilon_{300} = 5000\ M^{-1}\ cm^{-1}$), with 1 equiv of $Pb(NO_3)_2$, was consistent with a bisthiolate ligated Pb^{2+} ion (*29*). The absorbance at 300 nm formed in the absence and presence of atmospheric O_2. The absorbance was observed in the presence of 10 mM $CaSO_4$, as well, with a cooperative binding isotherm. The cooperative response (positive cooperativity) suggests that 10 mM Ca^{2+} ions competitively perturb Pb^{2+} ion binding above 5 μM by this absorbance assay. Using the more sensitive CdSe@ZnS nanoparticle-based biosensor (next section) this Ca^{2+} ion perturbation affects a submicromolar affinity phase but not a subnanomolar affinity phase. Thus, the observed absorbance-based cooperativity comes from the Pb^{2+} ion-bound products of these phases having similar optical signatures. Overall, PBP•Pb^{2+} was found to bind Pb^{2+} ions in the presence and absence of Ca^{2+} ions.

CdSe@ZnS Nanoparticle-Based Biosensors. Estimation of Pb^{2+} ion affinity and lower limit of detection for PBP•Pb^{2+} was performed using a semiconductor nanoparticle-based biosensor system. For this experiment, three different PBP•Pb^{2+}-MT constructs were generated with a single surface

Table 1: Pb^{2+} Ion Response of CdSe@ZnS Nanoparticle-Based Biosensors

		−$CaCl_2$						+10 mM $CaCl_2$					
complex **1** attachment site[a]	% quench (±**1**)[b]	% quench (±Pb^{2+})[c]	K_{D1} (nM)	A_1[d] (%)	K_{D2} (nM)	A_2[d] (%)	R	% quench (±Pb^{2+})[c]	K_{D1} (nM)	A_1[d] (%)	K_{D2} (nM)	A_2[d] (%)	R
K98C	15	59	1	45	200	55	0.989	47	1	45	100	55	0.992
N158C	13	78	1	20	200	80	0.995	45	1	50	100	50	0.986
A182C	18	21	1	30	800	70	0.974	54	1	50	100	50	0.996

[a] Surface cysteine mutant of PBP·Pb^{2+}-MT, where complex **1** was attached, used for experiments; $n = 3$ for all determinations. [b] Calculated as the emission intensity of **1**-modified PBP·Pb^{2+}-MT attached CdSe@ZnS nanoparticles divided by unmodified PBP·Pb^{2+}-MT attached CdSe@ZnS nanoparticles. [c] Calculated as the emission intensity of **1**-modified PBP·Pb^{2+}-MT attached CdSe@ZnS nanoparticles with 50 μM $Pb(NO_3)_2$ divided by emission intensity with no $Pb(NO_3)_2$. [d] Amplitude of each phase, where $A_1 + A_2 = 1$.

Cys mutation (K98C, N158C, and A182C). The surface Cys mutation allowed complex **1** (Scheme 1B, top) to be attached, while the MT domain allowed MHDA-capped CdSe@ZnS nanoparticle attachment (*20*). Each of these three proteins were separately expressed, purified, and modified with complex **1**, termed **1**-modified xxC PBP·Pb^{2+}-MT, where xxC denotes the surface Cys mutation. The MHDA-capping groups did not maintain nanoparticle solubility in the presence of 10 μM $Pb(NO_3)_2$ or 2 mM $CaSO_4$, so the PBP·Pb^{2+}-MT-attached MHDA-capped CdSe@ZnS nanoparticles were exchanged with MT peptides to replace the MHDA capping groups. Control experiments with MHDA-capped CdSe@ZnS nanoparticles verified previous reports of Pb^{2+} ion-induced precipitation of CdSe nanoparticles (*38*). The production of MT peptides and exchange with MHDA-capped CdSe@ZnS nanoparticles have been reported (*24*). While MT peptide capping groups provided a solution to $Pb(NO_3)_2$-mediated precipitation, additional capping groups are being explored to maintain biosensor solubility. The final construct examined in this report is a **1**-modified PBP·Pb^{2+}-MT adsorbed to MT-capped CdSe@ZnS nanoparticles. The quantum yield of these constructs varied between 15% and 20%. For brevity, this construct will be referred to as the CdSe@ZnS nanoparticle-based biosensor denoting the mutation (K98C, N158C, and A182C) with complex **1** attached (**1**-modified) or whether complex **1** was not attached using PBP·Pb^{2+}-MT (unmodified).

A 100 pM $Pb(NO_3)_2$ lower limit of detection was observed with the CdSe@ZnS nanoparticle-based biosensors. The nitrate salt of Pb^{2+} ions was specifically used, due to the weak counterion association of this salt and to provide a calibration curve for the response to exchangeable Pb^{2+} ions in solution. Addition of 50 μM $Pb(NO_3)_2$ to the CdSe@ZnS nanoparticle-based biosensors (5 nM) resulted in a 0.5−2.0-fold decrease (Table 1) in emission intensity at 545 nm (N158C, Figure 2A), where less than a 1.05-fold decrease was observed with unmodified CdSe@ZnS nanoparticle-based biosensors. Titrations of $Pb(NO_3)_2$ to the CdSe@ZnS nanoparticle-based biosensors (Figure 2) were best fit to a binding isotherm with two independent binding events. For example, the N158C CdSe@ZnS nanoparticle-based biosensor showed a high-affinity binding event with an association constant of 1×10^9 M^{-1} and a weaker binding event that was dependent on Ca^{2+} ions (no Ca^{2+} ions, 3.6×10^6 M^{-1}, 80% of amplitude change; 10 mM $CaSO_4$, 1×10^7 M^{-1}, 50% of amplitude change). No major change in quenching efficiency and Pb^{2+} ion-mediated emission responses was observed, with only a slight variation in the sample-to-sample response (error bars, Figure 2B−D). The complex **1** position-independent fluorescence response is

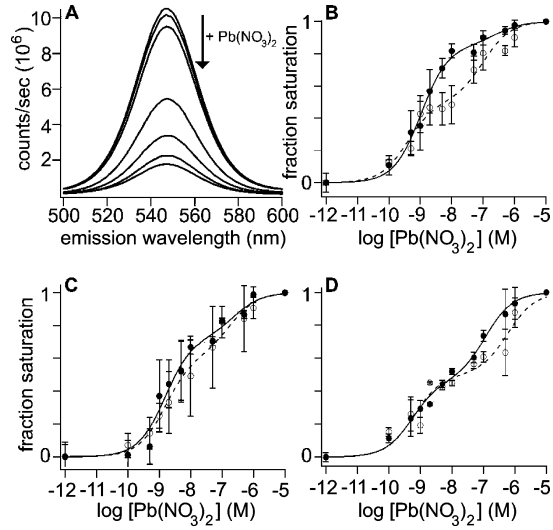

FIGURE 2: $Pb(NO_3)_2$-mediated fluorescence intensity changes with **1**-modified CdSe@ZnS nanoparticle-based biosensors (5 nM; A and B, N158C; C, K98C; D, A182C). (A) Spectra (0 nM, 0.5 nM, 1 nM, 10 nM, 100 nM, 1 μM, 5 μM). (B−D) Binding isotherm from emission intensities fit to two binding events (Table 1) for non-Ca^{2+} samples (filled circles, solid line) and Ca^{2+} samples (open circles, dashed line).

similar to the MBP analogue of these CdSe@ZnS nanoparticle-based biosensors (*20, 39*). The modular response with respect to attachment position further highlights that extensive Cys scanning mutagenesis is not necessary, as opposed to organic fluorophore modified proteins (*40*), for this class of biosensors (*19, 20, 39*). The uniformity of this response, with respect to complex **1** attachment position, is currently under investigation in our laboratory. However, the uniform response also led to each of the CdSe@ZnS nanoparticle-based biosensors with a lower $Pb(NO_3)_2$ detection limit of 100 pM (with or without 10 mM $CaSO_4$), except for K98C without Ca^{2+} ions which was 500 pM.

The weaker affinity Pb^{2+} ion-binding phase of the CdSe@ZnS nanoparticle-based biosensors had variable amplitudes in the absence of $CaSO_4$ but similar amplitudes in 10 mM $CaSO_4$ (Table 1). This result suggests that the $CaSO_4$-mediated cooperative Pb^{2+} ion absorbance response (Figure 1) is related to the weaker affinity binding phase rather than the high-affinity binding phase. On the basis of the absorbance and CdSe@ZnS nanoparticle-based emission responses, we assume the designed binding site of PBP·Pb^{2+} is successively binding two Pb^{2+} ions. In this model, the high-affinity phase forms a mononuclear Pb^{2+} site and the weaker affinity phase forms a binuclear Pb^{2+} site. Transitions from monomeric to dimeric Pb^{2+} ion complexes are known to occur in the solid state (*41*), and a similar coordination

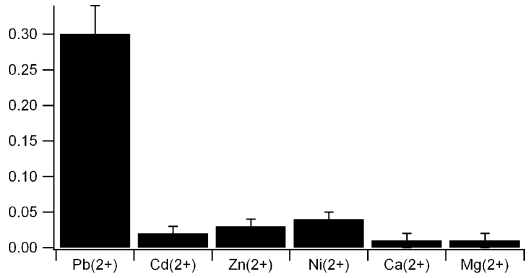

FIGURE 3: Selectivity of N158C biosensor system with CdSe@ZnS nanoparticles. The % quenching in emission intensity is reported after the addition of metal salts (Pb^{2+}, 500 pM $Pb(NO_3)_2$; Cd^{2+}, 100 μM $CdCl_2$; Zn^{2+}, 100μM $ZnCl_2$; Ni^{2+}, 100 μM $NiCl_2$; Ca^{2+}, 10 mM $CaSO_4$; Mg^{2+}, 10 mM $MgSO_4$). Hg^{2+} and Cu^{2+} salts are not reported in this figure due to these ions quenching emission from MT-capped CdSe@ZnS *without* **1**-modified PBP·Pb^{2+}-MT attached to it. See text for additional details.

sphere expansion was observed in a designed dinuclear Cu binding site in MBP (*42*). Such a dinuclear Pb^{2+} site was not designed but could further perturb the PBP·Pb^{2+} conformation (increased CdSe@ZnS nanoparticle quenching) and allow Ca^{2+} ions to perturb formation of this complex. Structural characterization is underway to better understand this weak-affinity binding phase in order to enhance the selectivity of the phase or eliminate it. For this weak-affinity phase (with and without 10 mM $CaSO_4$), the upper limit of $Pb(NO_3)_2$ detection is 1 μM with 5 nM CdSe@ZnS-based biosensors that provide a dynamic range from 100 pM to 1 μM.

The N158C CdSe@ZnS nanoparticle-based biosensor was selected for further characterization, and the metal ion specificity was examined. The selection of the N158C system was due the large high-affinity Pb^{2+} ion-dependent emission response relative to the A182C and K98C systems. No response was seen with the addition of $CaSO_4$, $MgSO_4$, $ZnCl_2$, $CdCl_2$, or $NiCl_2$, where a response was observed with the addition of 500 pM $Pb(NO_3)_2$ (Figure 3). These observations demonstrate a metal ion selectivity ($K_{Pb^{2+}}/K_{M^{2+}}$) of over 10^8 for Ca^{2+} ions and 10^6 for Zn^{2+}, Cd^{2+}, and Ni^{2+} ions. Addition of Cu^{2+}, Co^{2+}, or Hg^{2+} ions (100 μM) to the N158C CdSe@ZnS nanoparticle-based biosensor showed greater than 50% quenching ($CuSO_4$, 95%; $CoSO_4$, 58%; $HgCl_2$, 98%) but was also observed with only MT-coated CdSe@ZnS nanoparticles ($CuSO_4$, 95%; $CoSO_4$, 18%; $HgCl_2$, 94%). The MT-coated CdSe@ZnS nanoparticle response suggests that Cu^{2+} and Hg^{2+} bind to surface-bound MTs and alter the CdSe@ZnS nanoparticle emission. Binding of Cu^{2+} and Hg^{2+} to MT is not surprising based on our observations on CdSe nanoparticles (*22*) and other studies (*43*) and represents a limitation of the current capping groups. We are developing capping ligands that maintain nanoparticle solubility at physiological concentrations of mono- and divalent cation salts, but MT-capped nanoparticles provide a Pb^{2+} ion biosensor with a 100 pM to 1 μM dynamic range that is selective against Ca^{2+} ions (10 mM), Zn^{2+} ions (100 μM), Cd^{2+} ions (100 μM), and Ni^{2+} ions (100 μM).

InGaP@ZnS Nanoparticle-Based Biosensors. Red-emitting InGaP@ZnS nanoparticles were used to demonstrate that Pb^{2+} ion biosensing occurs with this preliminary system in the presence of red blood cells. The InGaP@ZnS nanoparticles replaced the CdSe@ZnS nanoparticles in the N158C CdSe@ZnS nanoparticle-based biosensor (N158C InGaP@ZnS nanoparticle-based biosensor). The parent InGaP@ZnS nanoparticles used for this study adsorb light with wavelengths at or shorter than 620 nm and have emission maxima around 660−670 nm (Scheme 1C, bottom). These characteristics remove interference from the major absorbance of hemoglobin (λ < 620 nm; $\varepsilon_{620,deoxy}$ = 5000 M^{-1} cm^{-1}, $\varepsilon_{620,oxy}$ = 1000 M^{-1} cm^{-1}) (*18*). Addition of the **1**-modified N158C PBP·Pb^{2+} to InGaP@ZnS nanoparticles caused a 15% quench in emission intensity (final quantum yield 4−8%), similar to the effect on CdSe@ZnS nanoparticle emission (13%). Upon addition of 50 μM $Pb(NO_3)_2$ to solutions of the N158C InGaP@ZnS nanoparticle-based biosensor (5 nM), a 70% quench was observed in the absence of $CaSO_4$ and a 45% quench was observed in the presence of 10 mM $CaSO_4$. $Pb(NO_3)_2$ titrations were performed as above using excitation wavelengths of 325 nm (InGaP@ZnS excitation maximum) and 620 nm to satisfy the red blood cell absorbance criterion (Figure 4). Lower limits of detection were found at 100 pM for both excitation wavelengths in buffer along with similar calculated affinities (K_{A1} = 1 × 10^9 M^{-1}, A_1 = 50%; K_{A2} = 1 × 10^7 M^{-1}, A_2 = 50%; R = 0.982) in the presence of 10 mM $CaSO_4$ (Figure 4C,D). This observation demonstrates that the observed modularity between CdSe@ZnS nanoparticle sizes (565 vs 545 nm emission) is maintained between nanoparticles of different semiconductors (CdSe@ZnS vs InGaP@ZnS nanoparticles).

The N158C InGaP@ZnS nanoparticle-based biosensor performance was examined in the presence of red blood cells. The concentration of the biosensor had to be increased to 200 nM for effective detection when mixed with red blood cells to provide a 1% hematocrit. These solutions were examined either in plastic 3 mL fluorescence cuvettes (fluorometer) or on microscope slides with coverslips

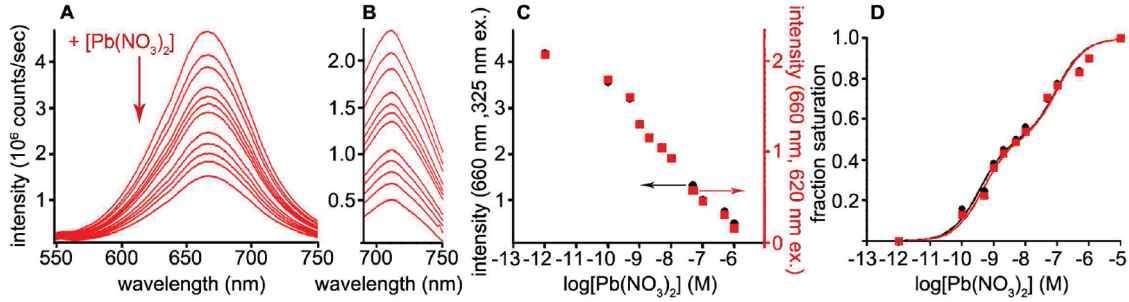

FIGURE 4: Pb^{2+} ion response to InGaP@ZnS nanoparticle-based biosensor (5 nM) in buffer. Fluorescence emission spectra were recorded with either 325 nm excitation (A) or 620 nm excitation (B) with the addition of various amounts of $Pb(NO_3)_2$. Isotherms of the emission response (C) and fraction signal saturation (D) to $Pb(NO_3)_2$ concentration gave similar responses with respect to excitation wavelength and CdSe@ZnS nanoparticle-based biosensors.

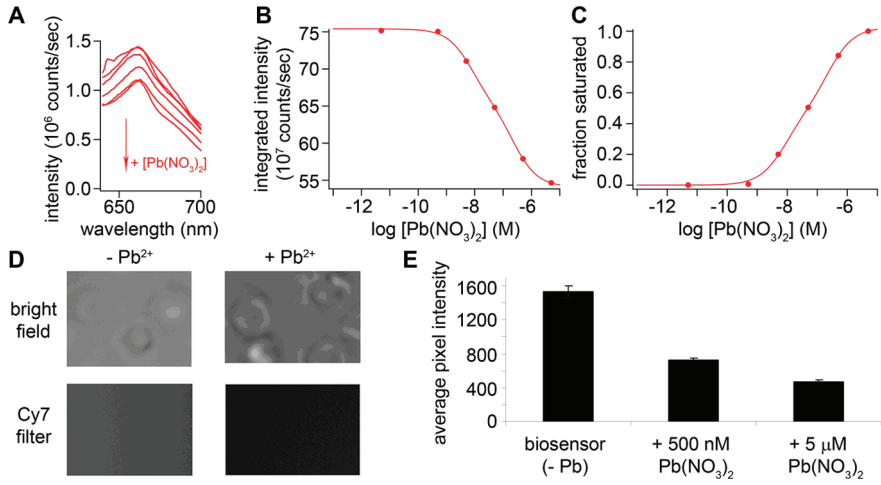

FIGURE 5: Pb^{2+} ion response to InGaP@ZnS nanoparticle-based biosensor (200 nM) in the presence of red blood cells (1% hematocrit). Samples were detected by fluorescence spectrophotometry (A−C, 20 nm slitwidths) or microscopy (D and E, Cy 7 filter). Emission intensities were integrated over the observed wavelength range (B, spectrophotometry) or taken as an average of pixel intensities (E, microscopy) and converted to fraction saturation to derive response functions with apparent association constants (C).

(fluorescence microscope). A 5 nM lower limit of detection was observed in this current system (Figure 5A−C) and can be lowered as larger InGaP@ZnS nanoparticles (red-shifted excitation and emission) are introduced to this system. Even with the increased detection limits in the presence of red blood cells, this observation demonstrates detection of Pb^{2+} ions far below other reported spectroscopic detection limits in the presence of red blood cells. The issue of biosensor solubility was addressed by fluorescence microscopy, where minimal variation in emission intensity was observed from the InGaP@ZnS nanoparticle-based biosensor in the presence of red blood cells (Figure 5D). Comparison of saturated Pb^{2+} ion responses between the plastic cuvette (26% quench) and microscope platforms (71% quench) demonstrates that necessity for increasing the biosensor concentration is primarily due to light scattering in the cuvette measurements. These findings demonstrate a biosensor that can detect Pb^{2+} ions at baseline levels detected in the plasma.

Use of this biosensor to detect Pb^{2+} ions in the presence of red blood cells is highly likely as well. Biosensor incorporation into red blood cells could be performed using the reversible pore-forming streptolysin-*o* as reported before (*44*). Clearly, the total Pb^{2+} ion concentrations will be in the micromolar range inside red blood cells; however, it is highly likely that the *exchangeable* Pb^{2+}ion concentrations will be in the current dynamic range of this biosensor. Biosensors that absorb and emit further into the near-infrared region could be generated using this method with larger InP@ZnS nanoparticles that have been recently reported (*14*). Coupling this biosensing technique with synchrotron X-ray fluorescence microscopy, as with Zn^{2+} ion distribution (*45*), would augment these measurements. Two extensions of the current biosensor are being developed to finalize detection in red blood cells, dual emission wavelength response for ratiometric detection and capping groups for improved nanoparticle solubility in physiological solutions. Therefore, this report details that the current biosensor provides a platform that will advance the study of Pb^{2+} ion interactions around and within red blood cells.

CONCLUSIONS

Structural parameters from low molecular weight metal complexes have been used in designing a Pb^{2+} ion binding protein that, when attached to complex **1** and a MT-capped CdSe@ZnS nanoparticle, functions as a fluorescent biosensor. Parameters were selected to favor stereochemcially active lone pair formation in the Pb^{2+} ion coordinated in this site. A strategy using ionic radii of metal ions for discrimination was not used since metal binding site plasticity could be introduced by domain−domain closure and flexible backbone positions in the loops making up the binding site. Admittedly, this strategy took advantage of a preexisting Arg residue from the phosphate binding site to potentially provide an electrostatic metal ion discrimination from non-SALP-forming metal ions. Further studies are underway for a better understanding of the selectivity provided by Arg 135 and the existence of a SALP in PBP•Pb^{2+}. Using this design strategy, a biosensor based on phosphate binding protein had a 100 pM $Pb(NO_3)_2$ lower limit of detection and a 100 pM to 1 μM dynamic range. The emission wavelength of the biosensor was altered from 545 to 660 nm by changing the nanomaterial from CdSe@ZnS to InGaP@ZnS. Use of InGaP@ZnS, and potentially larger InP@ZnS nanoparticles (*14*), allows Pb^{2+} ion detection in the presence of red blood cells (5 nM lower limit of detection). In light of the parent maltose biosensor system (*20, 39*), this report shows that CdSe@ZnS nanoparticle-based biosensors have a significant receptor modularity. The semiconductor modularity of the parent system was shown in translating the response readout from 545 nm emitting CdSe@ZnS nanoparticles to 660 nm emitting InGaP@ZnS nanoparticles. This designed protein demonstrates a highly sensitive and selective biosensor that can reversibly detect Pb^{2+} ions in aqueous solutions. Thus, the modularity of semiconductor nanoparticle-based biosensors has allowed metalloprotein design and different semiconductor materials to be combined to significantly improve the detection of soluble, exchangeable Pb^{2+} ion concentrations to address inefficient Pb^{2+} ion chelation therapy.

ACKNOWLEDGMENT

The authors acknowledge Prof. Dana Spence for use of red blood cells for this research.

SUPPORTING INFORMATION AVAILABLE

Design criteria/parameters for metalloprotein prediction, circular dichroism results, and CdSe@ZnS nanoparticle precipitation studies. This material is available free of charge via the Internet at http://pubs.acs.org.

REFERENCES

1. Department of Health and Human Services and Prevention, Center for Disease Control (2003) Surveillance for Elevated Blood Lead Levels Among Children—United States, 1997−2001, *Morbidity and Mortality Weekly Rep. 52*, 1−11.
2. Hamidinia, S. A., Erdahl, W. L., Chapman, C. J., Steinbaugh, G. E., Taylor, R. W., and Pfeiffer, D. R. (2006) Monensin improves the effectiveness of meso-dimercaptosuccinate when used to treat lead intoxication in rats. *Environ. Health Perspect. 114*, 484–493.
3. Smith, D., Hernandez-Avila, M., Tellez-Rojo, M. M., Mercado, A., and Hu, H. (2002) The relationship between lead in plasma and whole blood in women. *Environ. Health Perspect. 110*, 263–268.
4. Wiechert, W., Schweissgut, O., Takanaga, H., and Frommer, W. B. (2007) Fluxomics: mass spectrometry versus quantitative imaging. *Curr. Opin. Plant Biol. 10*, 323–330.
5. Lalonde, S., Ehrhardt, D. W., and Frommer, W. B. (2005) Shining light on signaling and metabolic networks by genetically encoded biosensors. *Curr. Opin. Plant Biol. 8*, 574–581.
6. Deuschle, K., Okumoto, S., Fehr, M., Looger, L. L., Kozhukh, L., and Frommer, W. B. (2005) Construction and optimization of a family of genetically encoded metabolite sensors by semirational protein engineering. *Protein Sci. 14*, 2304–2314.
7. Michalet, X., Pinaud, F. F., Bentolila, L. A., Tsay, J. M., Doose, S., Li, J. J., Sundaresan, G., Wu, A. M., Gambhir, S. S., and Weiss, S. (2005) Quantum dots for live cells, in vivo imaging, and diagnostics. *Science 307*, 538–544.
8. Gao, X., Chung, L. W. K., and Nie, S. (2007) Quantum dots for in vivo molecular and cellular imaging. *Methods Mol. Biol. 374*, 135–145.
9. Vinayakan, R., Shanmugapriya, T., Nair, P. V., Ramamurthy, P., and Thomas, K. G. (2007) An approach for optimizing the shell thickness of core-shell quantum dots using photoinduced charge transfer. *J. Phys. Chem. C 111*, 10146–10149.
10. Sandros, M., Behrendt, M., Maysinger, D., and Tabrizian, M. (2007) InGaP@ZnS-enriched chitosan nanoparticles: A versatile fluorescent probe for deep-tissue imaging. *Adv. Funct. Mater. 17*, 3724–3730.
11. Pradhan, N., Battaglia, D. M., Liu, Y., and Peng, X. (2007) Efficient, stable, small, and water-soluble doped ZnSe nanocrystal emitters as non-cadmium biomedical labels. *Nano Lett. 7*, 312–317.
12. Pradhan, N., and Peng, X. (2007) Efficient and color-tunable Mn-doped ZnSe nanocrystal emitters: Control of optical performance via greener synthetic chemistry. *J. Am. Chem. Soc. 129*, 3339–3347.
13. Gerbec, J. A., Magana, D., Washington, A., and Strouse, G. F. (2005) Microwave-enhanced reaction rates for nanoparticle synthesis. *J. Am. Chem. Soc. 127*, 15791–15800.
14. Xie, R., Battaglia, D., and Peng, X. (2007) Colloidal InP nanocrystals as efficient emitters covering blue to near-infrared. *J. Am. Chem. Soc. 129*, 15432–15433.
15. Domaille, D. W., Que, E. L., and Chang, C. J. (2008) Synthetic fluorescent sensors for studying the cell biology of metals. *Nat. Chem. Biol. 4*, 168–175.
16. Deo, S., and Godwin, H. A. (2000) A selective, ratiometric fluorescent sensor for Pb^{2+}. *J. Am. Chem. Soc. 122*, 174–175.
17. Chen, P., Greenberg, B., Taghavi, S., Romano, C., van der Lelie, D., and He, C. (2005) An exceptionally selective lead(II)-regulatory protein from Ralstonia metallidurans: Development of a fluorescent lead(II) probe. *Angew. Chem., Int. Ed. 44*, 2715–2719.
18. Antonini, E., and Brunori, M. (1971) *Hemoglobin and myoglobin in their reactions with ligands*, North Holland, Amsterdam.
19. Aryal, B. P., and Benson, D. E. (2006) Electron donor solvent effects provide semiconducting nanoparticle-based biosensors. *J. Am. Chem. Soc. 128*, 15986–15987.
20. Sandros, M. G., Gao, D., and Benson, D. E. (2005) A modular nanoparticle-based system for reagentless small molecule biosensing. *J. Am. Chem. Soc. 127*, 12198–12199.
21. Moschou, E. A., Bachas, L. G., and Deo, S. K. (2006) Hinge-motion binding proteins: Unraveling their analytical potential. *Anal. Chem. 78*, 6692–6700.
22. Aryal, B. P., and Benson, D. E. (2007) Polyhistidine fusion proteins can nucleate the growth of CdSe nanoparticles. *Bioconjugate Chem. 18*, 585–589.
23. Sandros, M. G., Gao, D., Gokdemir, C., and Benson, D. E. (2005) General, high-affinity approach for the synthesis of fluorophore appended protein nanoparticle assemblies. *Chem. Commun.,* 2832–2834.
24. Aryal, B. P., Neupane, K. P., and Sandros, M. G. (2006) Metallothioneins initiate semiconducting nanoparticle cellular toxicity. *Small 2*, 1159–1163.
25. Richardson, D. C., and Richardson, J. S. (1992) The kinemage: a tool for scientific communication. *Protein Sci. 1*, 3–9.
26. Ghosh, D., and Pecoraro, V. L. (2005) Probing metal-protein interactions using a de novo design approach. *Curr. Opin. Chem. Biol. 9*, 97–103.
27. Letondor, C., and Ward, T. R. (2006) Artificial metalloenzymes for enantioselective catalysis: Recent advances. *ChemBioChem 7*, 1845–1852.
28. Gillespie, R. J., and Nyholm, R. S. (1957) Inorganic stereochemistry. *Q. Rev. London 11*, 339–380.
29. Claudio, E. S., Godwin, H. A., and Magyar, J. S. (2003) Fundamental coordination chemistry, environmental chemistry, and biochemistry of lead(II). *Prog. Inorg. Chem. 51*, 1–144.
30. Hancock, R. D., Reibenspies, J. H., and Maumela, H. (2004) Structural effects of the lone pair on lead(II), and parallels with the coordination geometry of mercury(II). Does the lone pair on lead(II) form H-bonds? Structures of the lead(II) and mercury(II) complexes of the pendant-donor macrocycle DOTAM (1,4,7,10-tetrakis(carbamoylmethyl)-1,4,7,10-tetraazacyclododecane). *Inorg. Chem. 43*, 2981–2987.
31. Chen, P. R., Wasinger, E. C., Zhao, J., van der Lelie, D., Chen, L. X., and He, C. (2007) Spectroscopic insights into lead(II) coordination by the selective lead(II)-binding protein PbrR691. *J. Am. Chem. Soc. 129*, 12530–12531.
32. Matzapetakis, M., Ghosh, D., Weng, T. C., Penner-Hahn, J. E., and Pecoraro, V. L. (2006) Peptidic models for the binding of Pb(II), Bi(III) and Cd(II) to mononuclear thiolate binding sites. *J. Biol. Inorg. Chem. 11*, 876–890.
33. Wang, Y., Hemmingsen, L., and Giedroc, D. P. (2005) Structural and functional characterization of Mycobacterium tuberculosis CmtR, a PbII/CdII-sensing SmtB/ArsR metalloregulatory repressor. *Biochemistry 44*, 8976–8988.
34. Quiocho, F. A., Spurlino, J. C., and Rodseth, L. E. (1997) Extensive features of tight oligosaccharide binding revealed in high-resolution structures of the maltodextrin transport/chemosensory receptor. *Structure 5*, 997–1015.
35. Tam, R., and Saier, M. H., Jr. (1993) Structural, functional, and evolutionary relationships among extracellular solute-binding receptors of bacteria. *Microbiol. Rev. 57*, 320–346.
36. Luecke, H., and Quiocho, F. A. (1990) High specificity of a phosphate-transport protein determined by hydrogen bonds. *Nature 347*, 402–406.
37. Pellissier, A., Bretonniere, Y., Chatterton, N., Pecaut, J., Delangle, P., and Mazzanti, M. (2007) Relating structural and thermodynamic effects of the Pb(II) lone pair: A new picolinate ligand designed to accommodate the Pb(II) lone pair leads to high stability and selectivity. *Inorg. Chem. 46*, 3714–3725.
38. Ali, E. M., Zheng, Y., Yu, H. H., and Ying, J. Y. (2007) Ultrasensitive Pb^{2+} detection by glutathione-capped quantum dots. *Anal. Chem. 79*, 9452–9458.
39. Sandros, M. G., Shete, V., and Benson, D. E. (2006) Selective, reversible, reagentless maltose biosensing with core-shell semiconducting nanoparticles. *Analyst 131*, 229–235.
40. Feltus, A., and Daunert, S. (2002) Genetic engineering of signaling molecules, in *Optical Biosensors: Present and Future* (Ligler, F. S., and Lowe Taitt, C. A., Eds.) pp 307−329, Elsevier, Amsterdam.
41. Magyar, J. S., Weng, T.-C., Stern, C. M., Dye, D. F., Rous, B. W., Payne, J. C., Bridgewater, B. M., Mijovilovich, A., Parkin, G., Zaleski, J. M., Penner-Hahn, J. E., and Godwin, H. A. (2005) Reexamination of lead(II) coordination preferences in sulfur-rich sites: Implications for a critical mechanism of lead poisoning. *J. Am. Chem. Soc. 127*, 9495–9505.
42. Benson, D. E., Haddy, A. E., and Hellinga, H. W. (2002) Converting a maltose receptor into a nascent binuclear copper oxygenase by computational design. *Biochemistry 41*, 3262–3269.

43. Chan, J. N., Huang, Z. Y., Merrifield, M. E., Salgado, M. T., and Stillman, M. J. (2002) Studies of metal binding reactions in metallothioneins by spectroscopic, molecular biology, and molecular modeling techniques. *Coord. Chem. Rev.,* 319–339.
44. Agrawal, A., and Nie, S. (2005) Real-time detection of single quantum dots inside living cells. *Proc. SPIE 5705*, 152–158.
45. Fahrni, C. J. (2007) Biological applications of X-ray fluorescence microscopy: Exploring the subcellular topography and speciation of transition metals. *Curr. Opin. Chem. Biol. 11*, 121–127.
46. Swearingen, C. B., Wernette, D. P., Cropek, D. M., Lu, Y., Sweedler, J. V., and Bohn, P. W. (2005) Immobilization of a catalytic DNA molecular beacon on Au for Pb(II) detection. *Anal. Chem. 77*, 442–448.
47. Xiao, Y., Rowe, A. A., and Plaxco, K. W. (2007) Electrochemical detection of parts-per-billion lead via an electrode-bound DNAzyme assembly. *J. Am. Chem. Soc. 129*, 262–263.
48. Medintz, I. L., and Deschamps, J. R. (2006) Maltose-binding protein: A versatile platform for prototyping biosensing. *Curr. Opin. Biotechnol. 17*, 17–27.
49. Dwyer, M. A., and Hellinga, H. W. (2004) Periplasmic binding proteins: A versatile superfamily for protein engineering. *Curr. Opin. Struct. Biol. 14*, 495–504.
50. Shimoni-Livny, L., Glusker, J. P., and Bock, C. W. (1998) Lone pair functionality in divalent lead compounds. *Inorg. Chem. 37*, 1853–1867.
51. Hellinga, H. W., and Richards, F. M. (1991) Construction of new ligand binding sites in proteins of known structure. I. Computer-aided modeling of sites with pre-defined geometry. *J. Mol. Biol. 222*, 763–785.

BI801777H